Electronic Supplementary Material (ESI) for Physical Chemistry Chemical Physics.

Role of coherent nuclear motion in ultrafast intersystem crossing of ruthenium complexes

Supplementary Information

JunWoo Kim,[‡a] Dong-gu Kang,[b] Sang Kyu Kim,[b] and Taiha Joo*[a]

[a]Department of Chemistry, Pohang University of Science and Technology (POSTECH), Pohang 37673, Korea.

[b]Department of Chemistry, KAIST, Daejeon 34141, Korea

[‡]Present address: Department of Chemistry, Princeton University, Princeton, New Jersey 08544, United States

*Email: thjoo@postech.ac.kr

Contents

Supplementary information 1. Transition absorption peak assignment

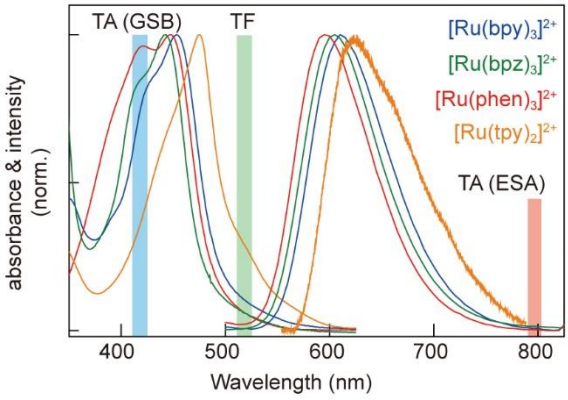

Fig. S1 Absorption and emission spectra of the four complexes. The detection wavelengths of the TA (GSB), TF, and TA (ESA) are marked as cyan, green, and red bars.

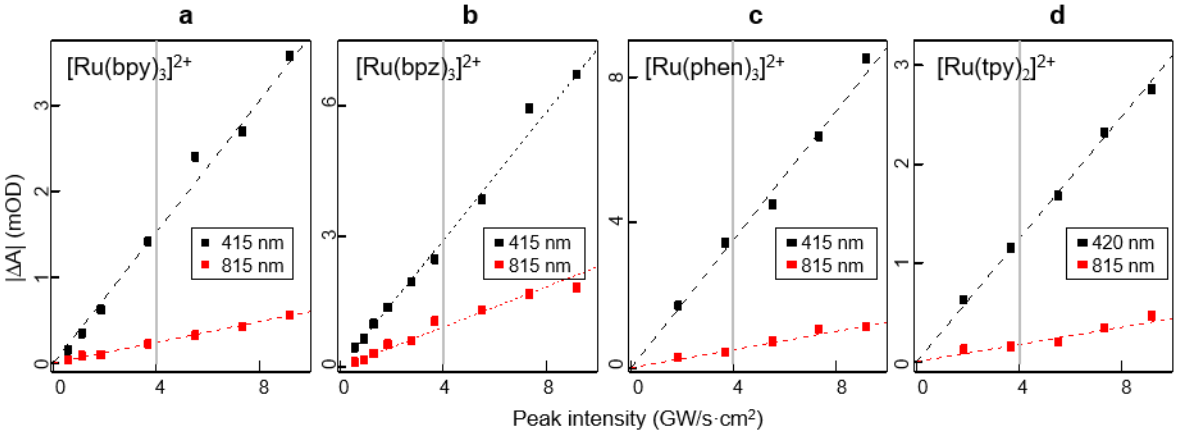

Fig. S2 Amplitudes of ^{1}MLCT (black square) and ^{3}MLCT (red square) peaks with various peak power of the pump pulses for (a) $[Ru(bpy)_3]^{2+}$, (b) $[Ru(bpz)_3]^{2+}$, (c) $[Ru(phen)_3]^{2+}$ (d) and $[Ru(tpy)_2]^{2+}$. Detection wavelengths are indicated in the legend. The dashed lines are the linear regression results. The gray lines represent the peak powers of the pump pulse chosen for the experiments in the main text.

In recent studies on femtosecond spectroscopy, the use of optical amplifier is necessary to achieve a successful wavelength conversion and a spectral broadening. The pulse energy of a seed pulse is usually amplified to a few millijoule level while reducing the repetition rate to several kHz. This condition is advantageous to enhance the signal-to-noise ratio (S/N). However, the extremely high peak power of an optical pulse interacting with a polyatomic molecules causes a multi-photon absorption, which may lead the system to be ionized or dissociated. As a result, the transition peaks originating from ions, radicals and/or fragments are often observed in optical-amplifier-based time-resolved spectra. We employed cavity-dumped Ti:sapphire laser rather than an optical amplifier to minimize such multi-photon effect. In order for proper peak assignment of ^{1}MLCT

and ^{3}MLCT, we measured transient absorption (TA) spectra of $[Ru(bpy)_3]^{2+}$, $[Ru(bpz)_3]^{2+}$, $[Ru(phen)_3]^{2+}$ and $[Ru(tpy)_2]^{2+}$, and observed the effect of pump power.

Fig. S2 shows pump power dependence on the TA signal amplitudes of $[Ru(bpy)_3]^{2+}$, $[Ru(bpz)_3]^{2+}$, $[Ru(phen)_3]^{2+}$ and $[Ru(tpy)_2]^{2+}$. The TA signal amplitudes detected at near-UV (415 nm) and at near-IR (815 nm) show excellent linearity with respect to the peak power of the pump, except the near-IR TA signal of $[Ru(bpz)_3]^{2+}$. If a peak induced by a multi-photon process are present in the detection peak, the TA amplitude must contain a component proportional to the higher order of the pump power. The near-IR TA signal of $[Ru(bpz)_3]^{2+}$ shows a relatively large amplitude ratio of near-IR to near-UV signals and the nonlinear power dependence. This may indicate that the characteristics of the near-IR band of $[Ru(bpz)_3]^{2+}$ is different from the near-IR TA signals of $[Ru(bpy)_3]^{2+}$, $[Ru(phen)_3]^{2+}$ and $[Ru(tpy)_2]^{2+}$.

Figs. S3 and S4 show the TA spectra of the four Ru(II) complexes at near-UV and near-IR regions, respectively. Firstly, the TA spectra at the near-UV region have the negative transient absorbance, and overlap well with the corresponding absorption spectra (Fig. S3). Additionally, we did not observe any population dynamics or spectral shift in the time window from 250 fs to 10 ps. This implies that there is no additional molecular dynamics that may influence the CVS analysis. Secondly, the TA spectra at the near-IR region are broad and have the positive transient absorbance (Fig. S4). While the near-IR TA spectra of $[Ru(bpy)_3]^{2+}$, $[Ru(phen)_3]^{2+}$ and $[Ru(tpy)_2]^{2+}$ have a band-like shape centered at 800 nm, the amplitude of the near-IR TA spectra of $[Ru(bpz)_3]^{2+}$ increases with wavelength. The near-IR TA spectra of $[Ru(bpy)_3]^{2+}$, $[Ru(phen)_3]^{2+}$ and $[Ru(tpy)_2]^{2+}$ also do not show any additional dynamics within 10 ps. Considering the structure-less feature and the nonlinear power dependence, it is difficult to conclude that the near-IR TA signal of $[Ru(bpz)_3]^{2+}$ originates from a single electronic (e.g. ^{3}MLCT) state, and, therefore, we did not use the $[Ru(bpz)_3]^{2+}$ results in the discussion.

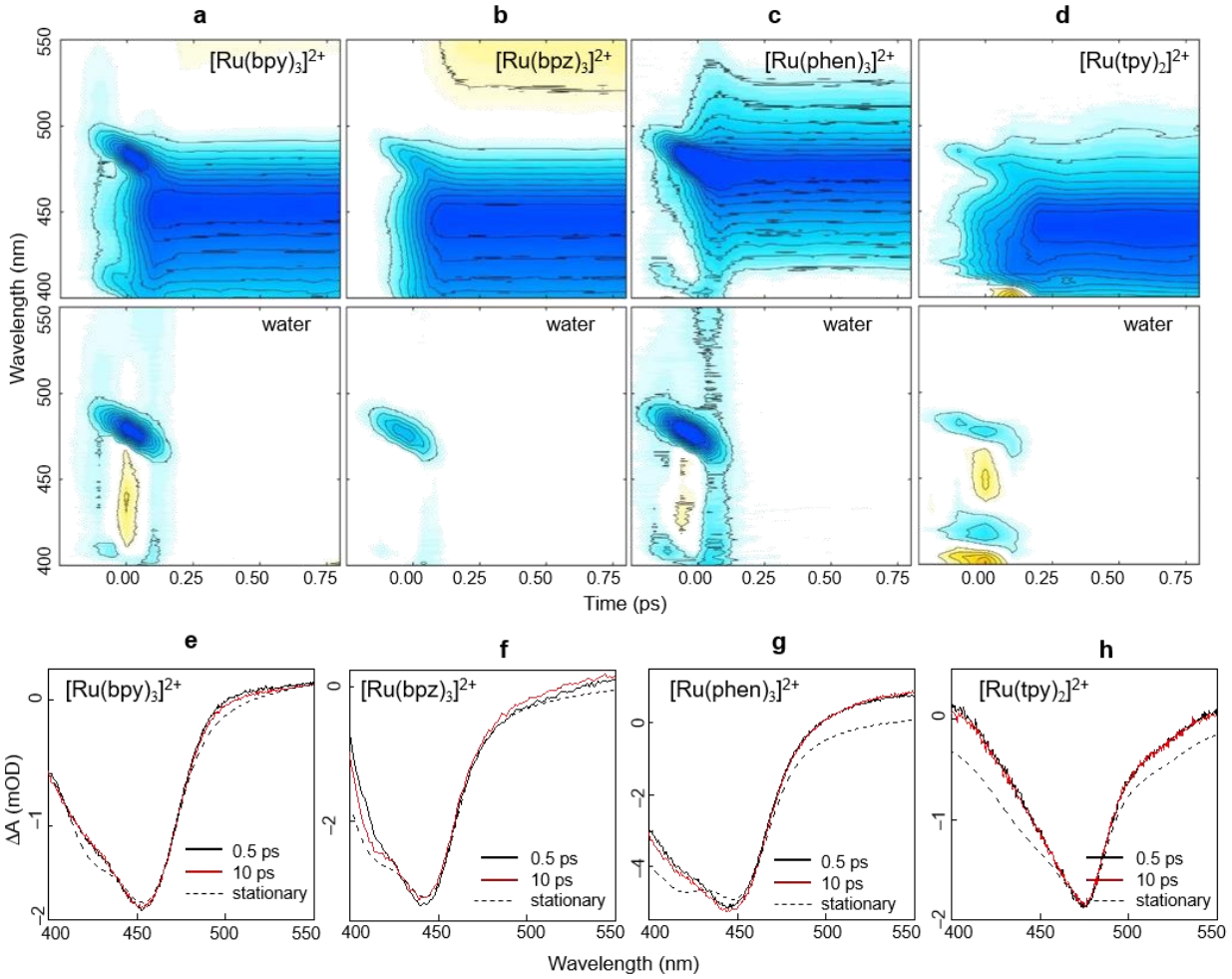

Fig. S3 The ground state bleach (GSB) spectra of (a) $[Ru(bpy)_3]^{2+}$, (b) $[Ru(bpz)_3]^{2+}$, (c) $[Ru(phen)_3]^{2+}$ and (d) $[Ru(tpy)_2]^{2+}$ solutions (upper panels), and the contribution of solvent in the spectra (lower panels). The GSB spectra of (e) $[Ru(bpy)_3]^{2+}$, (f) $[Ru(bpz)_3]^{2+}$, (g) $[Ru(phen)_3]^{2+}$ and (h) $[Ru(tpy)_2]^{2+}$ solutions at 0.5 ps (black) and 10 ps (red). The dashed lines are the absorption spectra of the corresponding compounds scaled by arbitrary constants.

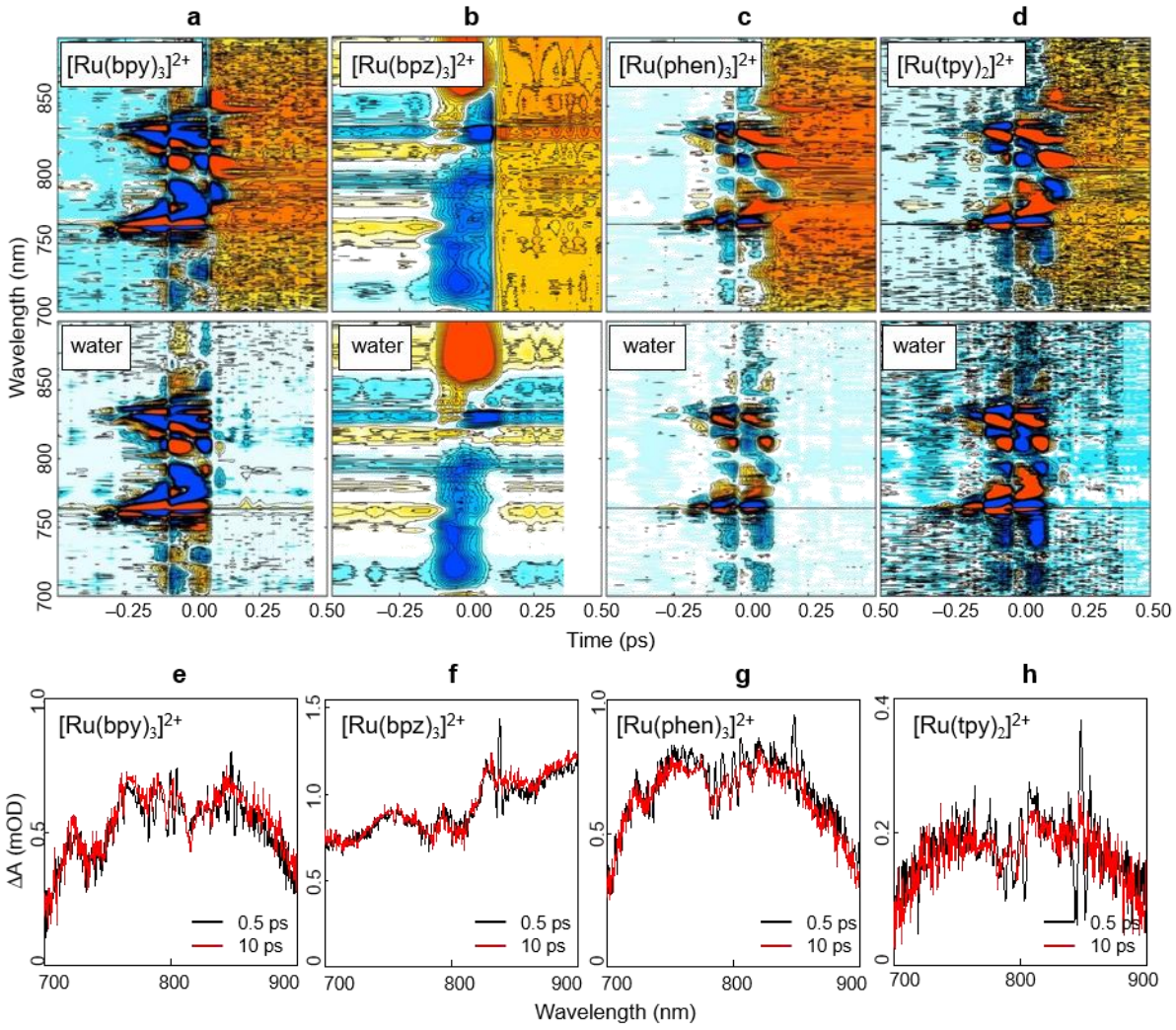

Fig. S4 The ESA spectra of (a) $[Ru(bpy)_3]^{2+}$, (b) $[Ru(bpz)_3]^{2+}$, (c) $[Ru(phen)_2]^{2+}$ and (d) $[Ru(tpy)_2]^{2+}$ solutions (upper panels), and the contribution of solvent in the spectra (lower panels). The ESA spectra of (e) $[Ru(bpy)_3]^{2+}$, (f) $[Ru(bpz)_3]^{2+}$, (g) $[Ru(phen)_2]^{2+}$ and (h) $[Ru(tpy)_2]^{2+}$ solutions at 0.5 ps (black) and 10 ps (red).

Supplementary information 2. Raw data of wave packet oscillations

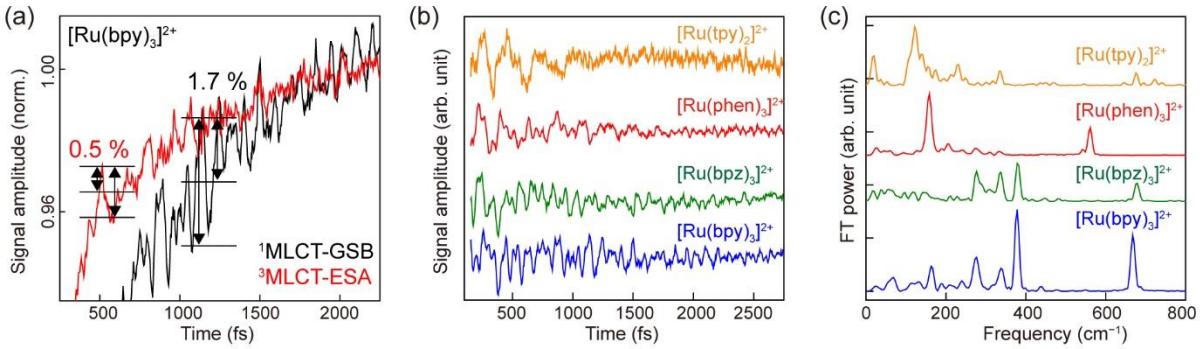

Fig. S5 Wave packet oscillations of the four Ru(II) complexes and their Fourier transforms. (a) The TA time profiles of the ^{1}MLCT-GSB at 415 nm (black) and ^{3}MLCT-ESA at 800 nm (red) of $[Ru(bpy)_3]^{2+}$. (b) The wave packet oscillations at the ^{1}MLCT-GSB bands of $[Ru(bpy)_3]^{2+}$, $[Ru(bpz)_3]^{2+}$, $[Ru(phen)_2]^{2+}$, and $[Ru(tpy)_2]^{2+}$ solutions, and (c) the Fourier transforms (CVSs) of them.

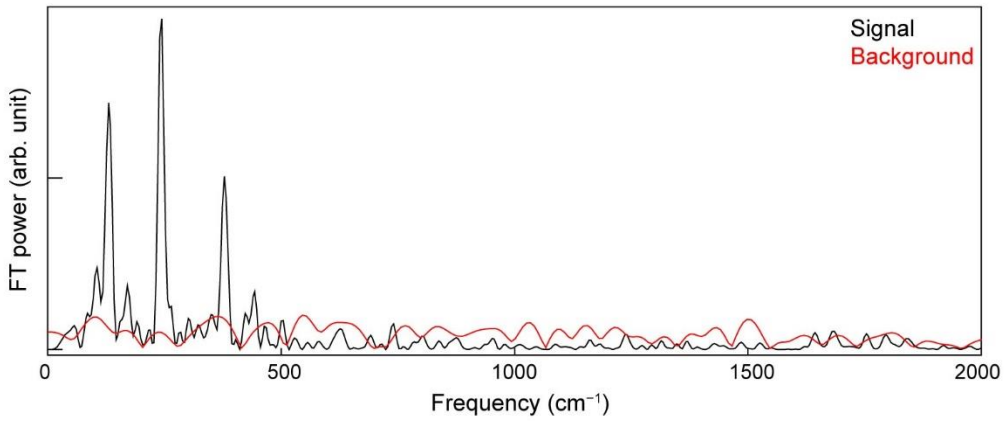

Fig. S6 Signal-to-noise ratio of CVS_t. Fourier power transform of the ^{3}MLCT-ESA signal acquired at negative time delay and time delay at >10 ps. CVS_t is also shown for comparison.

In order for the quantitative confirmation of a signal, the signal must be approximately three times more intense than noise level. As shown in Fig. S5a, the wave-packet-oscillation amplitude of ^{3}MLCT-ESA is much smaller than that of ^{1}MLCT-GSB. This implies that if an oscillatory noise presents in a TA data set, the noise can appear as a peak in CVS. Fig. S6a shows the time-profiles of ^{3}MLCT-ESA at $T > 160$ fs (black) and at $T < 0$ (red, $T = T + 450$ fs), where exponentially changing parts are eliminated by a nonlinear least-square fitting, and their Fourier transforms are depicted in Fig. S6a. The Fourier amplitude of the noise part (red) is scaled by a factor that is the square root of N_{noise}/N_{sig}, because the Fourier amplitude noise N_{noise} (N_{sig}) indicates the number of noise (signal) data points. It can be seen that the maximum noise level is comparable to the maximum signal level at the frequency region > 1000 cm^{-1}, where no wave packet oscillation is expected due to the limited time-resolution. The background spectra of three data sets (red, blue, and green in Fig. S6b) refer that there is no regular oscillating noise source.

Supplementary information 3. CVS simulation

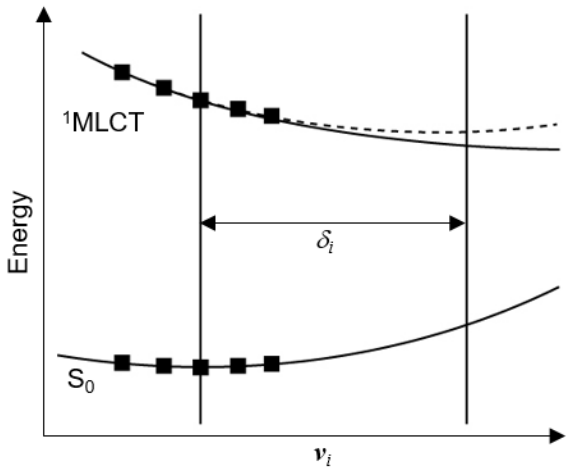

Fig. S7 The schematic diagram to demonstrate the simulation of CVS. The dashed line indicates the polynomial fit from the five data points of ^{1}MLCT. δ_i is the displacement of vibrational mode i, where ν_i indicates the corresponding vibrational coordinate.

We assumed that the normal modes of the ground and the excited states are the same. Under the assumption, the displacement between the two states of mode i (δ_i) can be numerically calculated as follow. First, the vibrational frequency (ν_i) and the coordinate ($\boldsymbol{\nu}_i$) were calculated by DFT calculation. The basis set was LANLDZ for Ru and 6-31g* for the other atoms. Effective core potential was employed for Ru atom. The exchange-correlation function was mPW1PW91. Second, single point calculations along $\boldsymbol{\nu}_i$ are performed (Fig. S7). The amount of the propagation length should be equivalent for every mode, so it was determined by the dimensionless displacement, which is defined as $\delta_{0,i} = \sqrt{\pi m_i \nu_i}$, where m_i is the reduced mass. Next, the ^{1}MLCT surface was expressed in quadratic form as

$$E_{e,i} = a_{e,i}\delta_{0,i}^2 + b_{e,i}\delta_{0,i} + c_{e,i}\,, \tag{S1}$$

where a, b and c are obtained by a polynomial fit. Finally, δ_i can be calculated as

$$\delta_i = \sqrt{\frac{b_{e,i}}{2a_{e,i}}}\,. \tag{S2}$$

Note that this expression is valid only for GSB, because δ_i varies with ν_i. The CVS calculation results are shown in Fig. 2 and Fig. S8 for $[Ru(bpy)_3]^{2+}$ and for $[Ru(bpz)_3]^{2+}$, $[Ru(phen)_3]^{2+}$, and $[Ru(tpy)_2]^{2+}$.

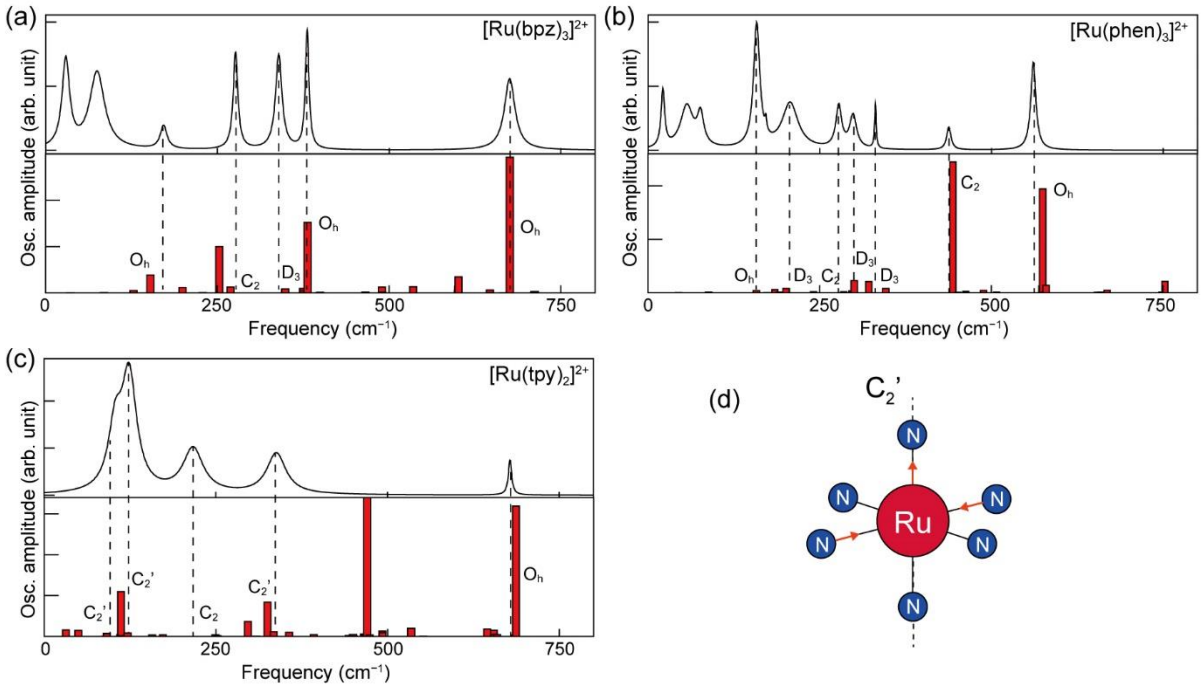

Fig. S8 The experimental CVS_s data (black lines) and simulation results (red bars) of (a) $[Ru(bpz)_3]^{2+}$, (b) $[Ru(phen)_3]^{2+}$ and (c) $[Ru(tpy)_2]^{2+}$. The point group represents the symmetry of each vibrational mode considering only the Ru and six N atoms. The nuclear motions of them are described in Fig. 5b in the manuscript. (d) The nuclear motion of C_2' modes shown in panel (c).

Table S1. Vibrational peak assignment comparison with previous studies

ν(CVSs) (cm^{-1})	|δ| (FT)	|δ| (LPSVD)	|δ| (Ref. 33)	Σ[a] (Table 1)	Σ[a] (Ref. 34)
122	0.29	0.71	-	D_3	-
163	0.35	0.41	-	O_h	-
249	0.23	0.40	-	D_3	-
276	0.29	0.39	0.25	D_3	D_3[b]
337	0.24	0.41	-	C_2	-
378	0.32	0.32	0.23	D_3	D_3[c]
669	0.27	0.26	0.437	O_h	O_h

[a]Point groups indicate the nuclear motion of RuN_6 as in Fig. 1d and Table 1.
[b]Two Ns in a bpy are moving away from each other, while their mean position is getting close to Ru.
[c]Two Ns in a bpy are moving away from each other.

Table S2. Configuration interaction coefficients of electronic transitions

		d_s-π*[a]	d_w-π*[a]	π-π*	*n*-π*
$[Ru(bpy)_3]^{2+}$	^{1}MLCT	0.98	-	-	-
	^{3}MLCT	0.24	0.14	0.52	-
$[Ru(bpz)_3]^{2+}$	^{1}MLCT	0.92	-	-	-
	^{3}MLCT	0.44	-	0.06	0.34
$[Ru(phen)_3]^{2+}$	^{1}MLCT	0.78	0.18	-	-
	^{3}MLCT	0.08	0.84	-	-
$[Ru(tpy)_2]^{2+}$	^{1}MLCT	0.80	0.16	-	-
	^{3}MLCT	0.56	0.40	-	-

[a]d_s (d_w) denotes *d*-orbital coupled strongly (weakly) to the ligand.

Supplementary Information 4. The error estimation in time-resolved fluorescence data fitting

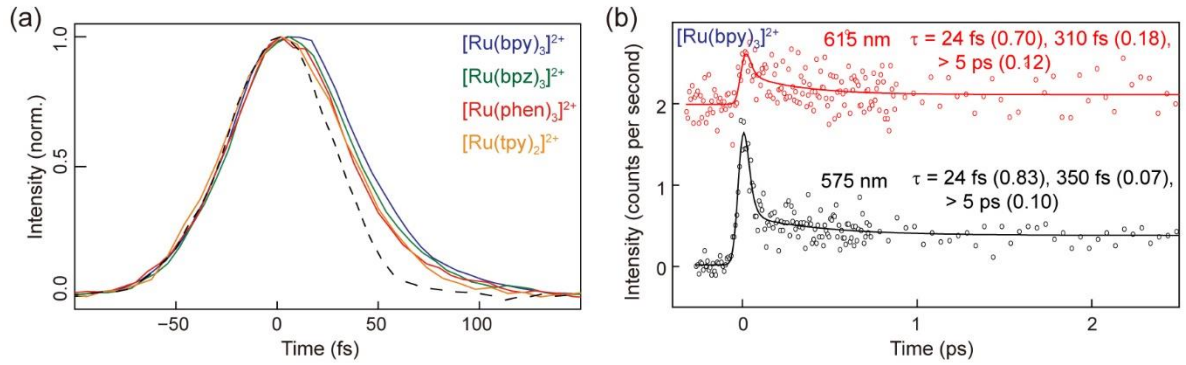

Fig. S9 (a) TF signals of $[Ru(bpy)_3]^{2+}$, $[Ru(bpz)_3]^{2+}$, $[Ru(phen)_3]_{2+}$, and $[Ru(tpy)_2]^{2+}$ at 510 nm (520 nm for $[Ru(tpy)_2]^{2+}$). The dashed line is the upconverted solvent (water) Raman signal representing the instrument response function (IRF). (b) TF signals of $[Ru(bpy)_3]^{2+}$ at 575 (black circles) and 615 nm (red circles), and their fitting results (full lines). τ indicates the decay-constants obtained from the fitting, and the numbers in the parentheses do the relative amplitudes of the decay components.

Time-resolved fluorescence (TF) shows the population dynamics of an excited state emitting the fluorescence, and it appears as an exponentially rise or decay time profile originating from population exchange or dynamic Stokes shift. Because any TF instrument has a limited time resolution, the population dynamics is recorded as a convoluted form considering the instrumental response function. Therefore, a deconvolution process is necessary for an accurate data analysis. When the population dynamics of interest is as fast as the instrumental response, the accuracy of the deconvolution method must be estimated.

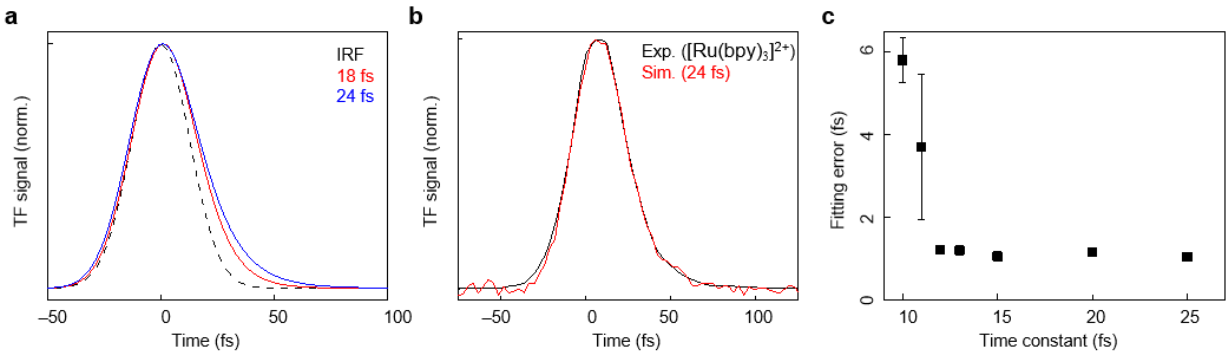

Fig. S10 TF fitting error estimation. (a) The convolution test with a Gaussian pulse of 60 fs FWHM (dashed line) and two exponentially decaying curves with time constants of 18 fs (red) and 24 fs (blue). (b) The experimental TF data of $[Ru(bpy)_3]^{2+}$ (black), and a convoluted decay curve with the time resolution of 60 fs, decay time of 24 fs and fluctuation amplitude of 0.015. (c) The estimated exponential fitting error as a function of time constant with the fluctuation amplitude of 0.015.

In this research, we utilized a TF instrument with the time-resolution of 60 fs in full-width half-maximum. All the TF data in this research were deconvoluted by non-linear least-square fitting methods with a convoluted exponential as a model function. As represented in Fig. S10a, the time-resolution of 60 fs is high enough to distinguish the fastest (18 fs) and slowest (24 fs) time constants mentioned in the main text in ideal case.

We performed a numerical simulation to estimate the systematic error applicable for our fitting result. First, we extracted the maximum-fluctuation-amplitude normalized by the signal maximum from the raw data. The extracted fluctuation amplitude was 0.015 in average. The raw TF data of $[Ru(bpy)_3]^{2+}$ (black) and a fluctuation-adapted simulated data with the time constant of 24 fs (red) are depicted in Fig. S10b. We made three hundred data sets for a time constant, and extracted fitting errors. Then, the fitting error ($\sigma_{\tau,sys}$) at a given time constant (τ) was estimated as

$$\sigma_{\tau,sys} = \left| \sum_{i=1}^{N} \frac{\tau_{fit,i} - \tau}{N} \right| + \sqrt{\sum_{i=1}^{N} \frac{\left(\tau_{fit,i} - \tau\right)^2}{N}} \,. \tag{S3}$$

$\tau_{fit,i}$ indicates the fit value of i-th data set. The first term in Eq. (S3) considers the drift of the fitting result, while the second terms does the statistic error. The calculated $\sigma_{\tau,sys}$ for several τ-values are plotted in Fig. S10c. According to our simulation result, the fitting error for our experimental condition (15 fs < τ < 25 fs, time-resolution: 60 fs) was approximately estimated to 1.1 fs. Finally, the total error ($\sigma_{\tau,tot}$) of our experiment should consider the statistic error ($\sigma_{\tau,st}$) as

$$\sigma_{\tau,tot} = \sqrt{\sigma_{\tau,st}^2 + \sigma_{\tau,sys}^2} \,. \tag{S4}$$

Here, $\sigma_{\tau,st}$ is the standard deviation of the fitting results of three independent TF measurements.